crystals

MDPI

Article

Improvement of Mechanical Properties for a Novel Zr–Ti–V Alloy via Hot-Rolling and Annealing Treatment

Yiwei Liu [1], Kai Chen [1], Tianshuo Song [1], Bohan Chen [2,3,*], Qiang Li [1] and Chaoqun Xia [1,3,*]

[1] Tianjin Key Laboratory of Materials Laminating Fabrication and Interface Control Technology, School of Materials Science and Engineering, Hebei University of Technology, Tianjin 300130, China
[2] Department of Mechanical Engineering, The Hong Kong Polytechnic University, Hong Kong, China
[3] State Key Laboratory of Metastable Materials Science and Technology, Yanshan University, Qinhuangdao 066004, China
* Correspondence: bohan.chen@polyu.edu.hk (B.C.); chaoqunxia@hebut.edu.cn (C.X.)

Abstract: In this experiment, an annealing treatment was carried out for a rolled Zr–Ti–8V alloy, and the toughening mechanism of the material was thoroughly analyzed by combining advanced material characterization and other testing methods. The phase composition of the Zr–Ti–8V alloy was sensitive to the applied annealing temperature, while a series of changes in the phase composition of the alloy were induced by enforcing bigger thermal budgets. Implementing a temperature value of 450 °C led to a higher α-phase content, in striking contrast with the case where a lower annealing temperature of 400 °C was applied. The β grains that were stretched in the alloy's rolling direction and annealed at 600 °C to 800 °C were recrystallized. As a result, the acquired configuration was equiaxed with β grains. The extracted results revealed that the alloy annealed at 450 °C showed a good strong–plastic ratio, with tensile strength and elongation of 1040 MPa and 8.2%, respectively. In addition, the alloy annealed at 700–800 °C showed good plasticity properties. From the hardness tests and friction wear experiments on all the experimental alloys, it was demonstrated that the dual-phase alloy with $\alpha + \beta$ had higher hardness and wear resistance, whereas the opposite trend was observed for the single β-phase alloy.

Keywords: Zr alloys; microstructure; tensile performance; tribological properties

Citation: Liu, Y.; Chen, K.; Song, T.; Chen, B.; Li, Q.; Xia, C. Improvement of Mechanical Properties for a Novel Zr–Ti–V Alloy via Hot-Rolling and Annealing Treatment. *Crystals* **2022**, *12*, 1765. https://doi.org/10.3390/cryst12121765

Academic Editors: Jun Tan and Quan Dong

Received: 26 October 2022
Accepted: 27 November 2022
Published: 5 December 2022

1. Introduction

Zirconium (Zr) and Zr-based alloys are regarded as excellent material structures for the nuclear industry [1–3]. More specifically, the relatively small neutron absorption cross-sectional area of the Zr-based materials reduces the imposed damages to the structural components in the irradiated environment, which in turn improves their material lifetime. Consequently, Zr and Zr-based alloys have applications of high importance in the nuclear industry, accounting for about 70% of their total production applications. Conventional Zr-based alloys have several disadvantages, such as low tensile strength and susceptibility to pitting, which significantly limit their application to other fields [4–6]. In addition to the nuclear industry, Zr and Zr-based alloys also have important applications in the aerospace field. However, there currently are not many Zr-based alloys that are commercially available. Due to the modern needs of both the nuclear and aerospace industries, the development of new Zr-based materials with high mechanical strength and corrosion resistance capable of adapting to the complex space environment has become a research hotspot [7,8]. The optimization of the composition of the material and enforcing different rolling deformation treatments for improving the alloy's strength has been reported in the literature. However, in the industrial field, in order to better adapt the structural material to the operating environment, it is necessary to apply a heating process during the synthesis of the structural material to obtain matching operating properties [9].

The desired microstructure of Zr-based alloys can be obtained by selecting the appropriate thermomechanical processing parameters (e.g., strain rate, deformation, and temperature) to acquire suitable properties [10]. Zhang et al. [11] first discovered the double yielding behavior in Zr-based alloys by examining the organization and mechanical properties of a new Zr–Al–V-based alloy in the hot-rolled state. The alloy can be rolled and deformed, which leads to an increase in the density of defects within the matrix and an elevated distortion of gold. As a result, the alloy exhibits mechanical instability [12–14]. Moreover, the β-phase volume fraction and grain size in the alloy increase with the annealing temperature, while the excessive grain size is not conducive to the overall mechanical properties of the alloy. Thus, the annealing temperature of Zr–Ti-based alloys should not be made too high [15,16].

After the plastic deformation region, the annealing process results in a more homogeneous organization and the formation of stable grain boundaries. To better understand the induced changes in the specimen's organization and the mechanical properties of the annealing process parameters, many experiments have been conducted [17,18]. Yang et al. [19] annealed a Zr–2.5Nb alloy in the hot-rolled state, and the results showed that the post-extension of the alloy gradually increased. The tensile strength also initially showed a tendency to increase and then decrease when annealed at 300–700 °C. By applying an annealing temperature of 500 °C, a β-phase to ω transition was recorded, which was the main goal for strengthening the alloy. In addition to the impact of the annealing temperature on the conventional mechanical properties of Zr-based alloys, the influence of the annealing temperature on the frictional properties of Zr-based alloys has been reported by a few studies in the literature. It is worth noting that zirconium and its compounds are used in medicine, particularly, the production of oxide structures with the high hardness and wear resistance of zirconium products [20,21]. Ding et al. [22] further improved the wear resistance and corrosion resistance of Zr–Ti-based alloy surfaces by using a thermal oxidation treatment. Wang et al. found the biomedical feasibility of Ti–Nb–Zr shape memory alloy through their research; more generally, these alloys are the basis for shape memory materials [23].

The addition of element V as an alloying element in zirconium alloys enhances plasticity, has a low rheological stress, and facilitates die forging. In our group's previous research, it was found that Zr–Ti–8V exhibited excellent performance. To further improve the strong plasticity of Zr-based alloys, this study explored the annealing of a hot-rolled Zr–Ti–8V alloy. The correlation between the different annealing temperatures on the mechanical properties of the proposed alloy structure, phase transformation and its tissue evolution pattern, plastic deformation, and work hardening were thoroughly investigated. Its tribological wear properties were also studied, as a lack of tribological behavior data would significantly limit its potential for use in moving parts.

2. Materials and Methods

The Zr–Ti–8V alloy was prepared in a vacuum induction suspension melting furnace by using a water-cooled copper crucible. The selected raw materials were 99.7% titanium sponge, 99.5% Zr sponge, and 99.9% high-purity vanadium lumps, added according to an atomic ratio of 23:23:4, with a total mass of approximately 5 kg. After the elapse of 30 min, the uniformly melted alloy was cast into alloy ingots. The ingots were cut into blocks of 20 mm height, 20 mm width, and 20 mm length blocks by wire cutting. The muffle furnace was first raised to a preset temperature, and then the blocks were placed in the muffle for 30 min at 550 °C and then immediately removed for rolling. The rolling was achieved with a two-high hot rolling mill. The method of multiple passes of late binding was used. The amount of down-pressing was 4 mm. After three instances of down-pressing, to avoid the alloy from cracking in the rolling process, the last amount of down-pressing was 2 mm. Finally, the sample was rolled from 20-mm-thick to 6-mm-thick sheets.

The hot-rolled samples were then placed in a vacuum tube furnace and were annealed at the following temperature values with a holding time of 3 h: 400 °C, 450 °C, 500 °C,

600 °C, 700 °C, and 800 °C. The cooling was performed by means of furnace cooling. Specimens were sanded with 150#, 600#, 1000#, 2000#, 3000#, and 5000# sandpaper, followed by polishing. The specimens were subjected to metallographic etching with Kroll reagent, which was composed of a mixture of H_2O, HNO_3, and HF (16:3:1). The phase composition of the samples was measured by X-ray diffraction (XRD, Bruker D8 Discover) at an angle of 10–90°. Optical microscopy (OM, OLYCIA M3), scanning electron microscopy (SEM, JEOL JSM-7100 (JEOL Ltd., Tokyo, Japan), electron probe (EPMA, JEOL JXA-8530F (JEOL Ltd.)), and transmission electron microscopy (TEM, JEOL-2010 (JEOL Ltd.)) measurements were used for microstructure and elemental distribution of the alloy. The TEM specimens were prepared via twin-jet electropolishing. The preparation environment was −30 °C, 15 V, at 10 wt% perchloric +90 wt% methanol electrolyte. The phase-transition temperature of the alloy was also tested by differential scanning calorimetry (DSC, TA Instruments SDT Q-600 (TA Instruments, New Castle, DE, USA)).

Hardness testing was carried out using an FM ARS 9000 micro-Vickers hardness tester from FUTURE-TECH (Kawasaki, Japan). The hardness test load was 200 gf for 15 s, whereas an average value was taken for 12 consecutive measurements. The tensile tests were carried out on an Instron5982 tester, all-sheet tensile samples were used, the length direction of the sample was in the rolling direction, and the test rate was 5×10^{-4} s^{-1}. To ensure the accuracy of the tests, three samples were prepared for testing.

Before conducting the friction and wear tests, the entire specimen was polished to exclude the influence of different surface roughness values on the test results. In this experiment, the reciprocating mode of the Bruker UMT-5 friction and wear tester were used for the dry friction test at room temperature under air condition. By applying a loading pressure of 10 N, a sliding speed of 1 cm/s, a reciprocating amplitude of 4 mm, and a sliding time of 10 min, the friction and wear were characterized by the reciprocation of linear sliding friction between the ball blocks. The indenter in the friction and wear test was a GCr15 steel ball.

3. Results

3.1. Initial Microstructure and Phase-Transition Temperature

Figure 1a,b depicts the EBSD graphics of the hot-rolled Zr–Ti–8V alloy. The results show that all grains of the hot-rolled Zr–Ti–8V alloy were compressed and deformed along the ND direction. Furthermore, a large amount of deformed fiber organization within the original β grains was captured in combination with a large amount of deformation weave inside the alloy. The presence of a deformation weave led to a change in the alloy crystallographic orientation. Figure 1c shows the acquired XRD pattern of the Zr–Ti–8V alloy in the rolled state. By observing the peak intensity of the (200) crystallographic diffraction peak at 2θ = 53° in the XRD diffraction pattern of Figure 1c, the peak intensity of the (200) crystallographic diffraction peak of the hot-rolled Zr–Ti–8V alloy is significantly higher than that of the other crystallographic orientations. This effect clearly indicates that the base crystal of the alloy has been selectively oriented during the applied rolling process.

The main methods that are commonly used in the laboratory to test the phase-transition temperature of alloys include metallographic and DSC methods. Compared with the metallographic method, DSC has the advantages of fast detection, high sensitivity, and low cost [24–26]. The phase-change point of the alloy was also tested. Since the Zr–Ti–8V alloy in the hot-rolled state could be found in full β-phase, the rolled state was regarded as the complete β phase, while the phase-transition point could not be obtained by the DSC test. For that reason, the alloy was held at 400 °C for 24 h before carrying out the phase-change point test. The extracted DSC results are shown in Figure 1d, where a single α-phase below 440 °C, a single β-phase above 510 °C, and a co-existence of the α + β phases in the middle of these two temperature ranges was detected.

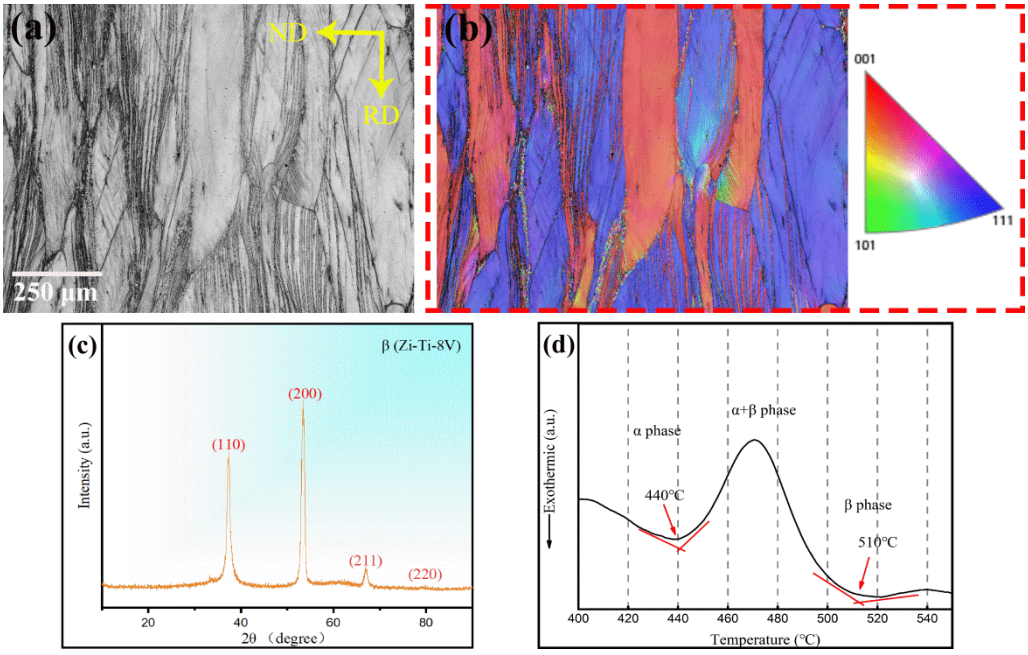

Figure 1. (**a**,**b**) EBSD orientation image of 450 °C of hot-rolled Zr–Ti–8V alloy; (**c**) XRD pattern of hot-rolled Zr–Ti–8V alloy; (**d**) DSC curve of Zr–Ti–8V alloy.

3.2. Phase Composition and Microstructure after Annealing

Figure 2 shows the XRD patterns and TEM images of the Zr–Ti–8V alloy in the rolled state at different annealing temperatures. As can be ascertained from Figure 2a, the phase composition of the Zr–Ti–8V alloy was changed significantly by enforcing different annealing temperatures. Partial enlargement of the XRD diffraction pattern of the Zr–Ti–8V alloy annealed at 400 °C, 450 °C, and 500 °C in the range of 50° to 60° was measured by observing the intensity of the diffraction peaks in the β-phase (200) plane. However, at the temperature values of 450 °C and 500 °C, the α-phase and β-phase contents of the alloy were diametrically opposed [27,28]. More specifically, the α-phase content predominated at 450 °C, and the β-phase content predominated at 500 °C. The phase-transition point of the Zr–Ti–8V alloy was reported in our previous work, in which it was demonstrated that the biphasic zone of the alloy was developed in the temperature range of 440 °C to 510 °C. The phase composition of the alloy annealed at 400 °C is biphasic mainly due to the weak atomic migration ability at this low temperature value and the short holding time. Consequently, the β-phase fails to decompose completely into the α-phase. Interestingly, above the temperature value of 600 °C, the phase composition of the alloy was mainly composed of a single β-phase, and no other phase structure was found. Figure 2b shows TEM images of the annealed alloys at 400 °C, 450 °C, and 500 °C, where the needle-like alpha phase is clearly visible in the matrix along a certain orientation.

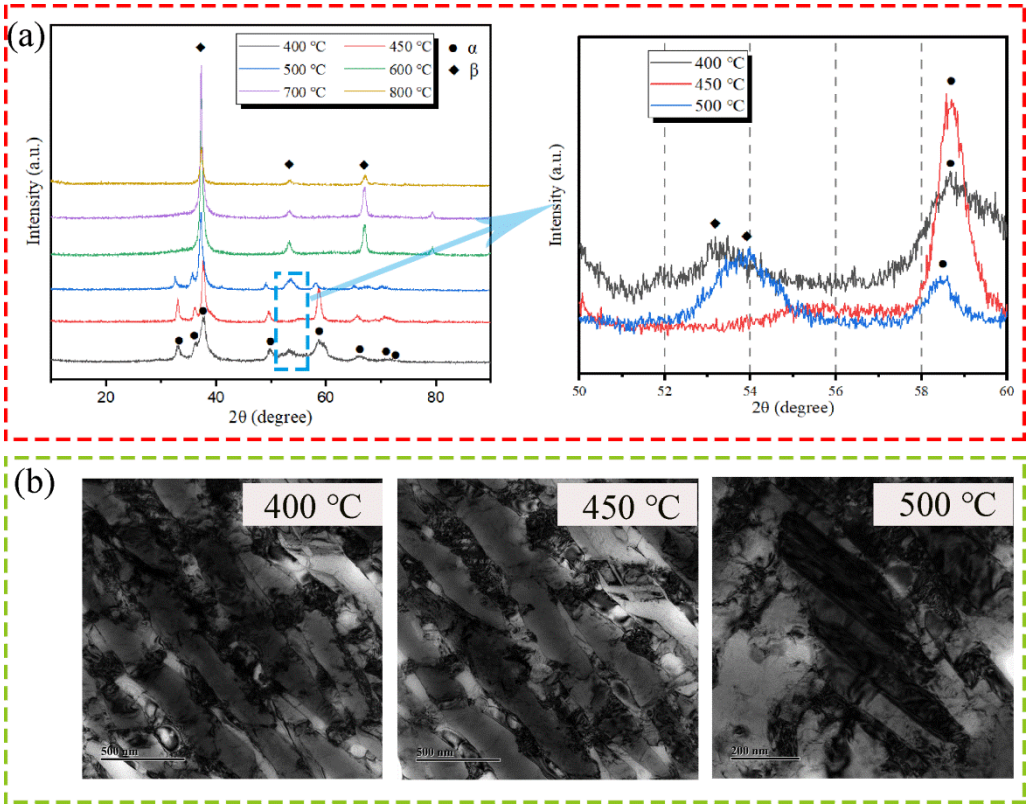

Figure 2. (**a**) XRD pattern of the annealed Zr–Ti–8V alloys; (**b**) TEM images of the Zr–Ti–8V annealed alloy at 400 °C, 450 °C, and 500 °C.

The microstructure images of the annealed Zr–Ti–8V alloy are shown in Figure 3. The alloy organization that is displayed in the metallographic image in Figure 3a was significantly influenced by the annealing temperature. At the temperature range of 400–500 °C, the alloy grain morphology remained the same as that after the rolling deformation process. Moreover, the equiaxed grains were stretched along the rolling direction, and a large number of stripes along the rolling direction were distributed inside the grains. Arguably, the internal stresses inside the annealed alloy do not disappear completely in this temperature range, whereas both the annealing temperature and time cannot induce the recrystallization of the alloy. By further observation of metallographic organization, it was found that regular precipitation of black tissue near the deformed tissue of grain boundaries occurred at the annealing temperatures of 400 °C and 450 °C. On the other hand, in the organization of the unknown region, annealing at 450 °C rather than 400 °C led to the precipitation of more tissue. At 500 °C, the precipitated tissues near the grain boundaries disappeared, but the grain boundaries and deformation stripes appear coarsened, probably due to the precipitation of other tissues in this area. Additionally, according to the XRD analysis, the precipitated structure may be composed of a fine needle-like α phase.

When the annealing temperature was increased above the value of 600 °C, the deformed grains and deformation streaks disappeared from the matrix, and a relatively large number of equiaxed β grains with uniform and small grain sizes appeared. By comparing the average grain size (600–800 °C annealed), it was found that the grain size of the sample annealed at 800 °C was the largest. From the SEM image shown in Figure 3b, substantial needle-like α-phase organization was detected at the annealing temperature values of 400 °C and 450 °C, whereas the needle-like α was regularly distributed in the matrix along with the deformed fiber organization. Annealing at 500 °C led to the formation of a small amount of needle-like α-phase precipitation on both sides of the grain boundary, which can be interpreted as the existence of a coarse grain boundary in the metallographic picture. Combined with the binary phase diagrams of Zr–V and Ti–V, the solid solubility of element

V in α-Ti and α-Zr is evidently limited. Therefore, the distribution of elements in the alloy microstructure must be further studied. Figure 3c shows the EBSD image of the alloy annealed at 450 °C, where the distribution of α and β phases in the matrix of the alloy annealed at 450 °C can be more clearly observed. Although the α phase precipitated in the β matrix, this precipitation was not uniform. Furthermore, the α phase precipitated only inside β grains, whereas some β grains were retained under the low-temperature annealing condition at 450 °C. This situation may be related to the solid solubility of V elements in the α phase and the aggregation of V elements within specific β grains that caused the inhomogeneity of the α phase precipitation.

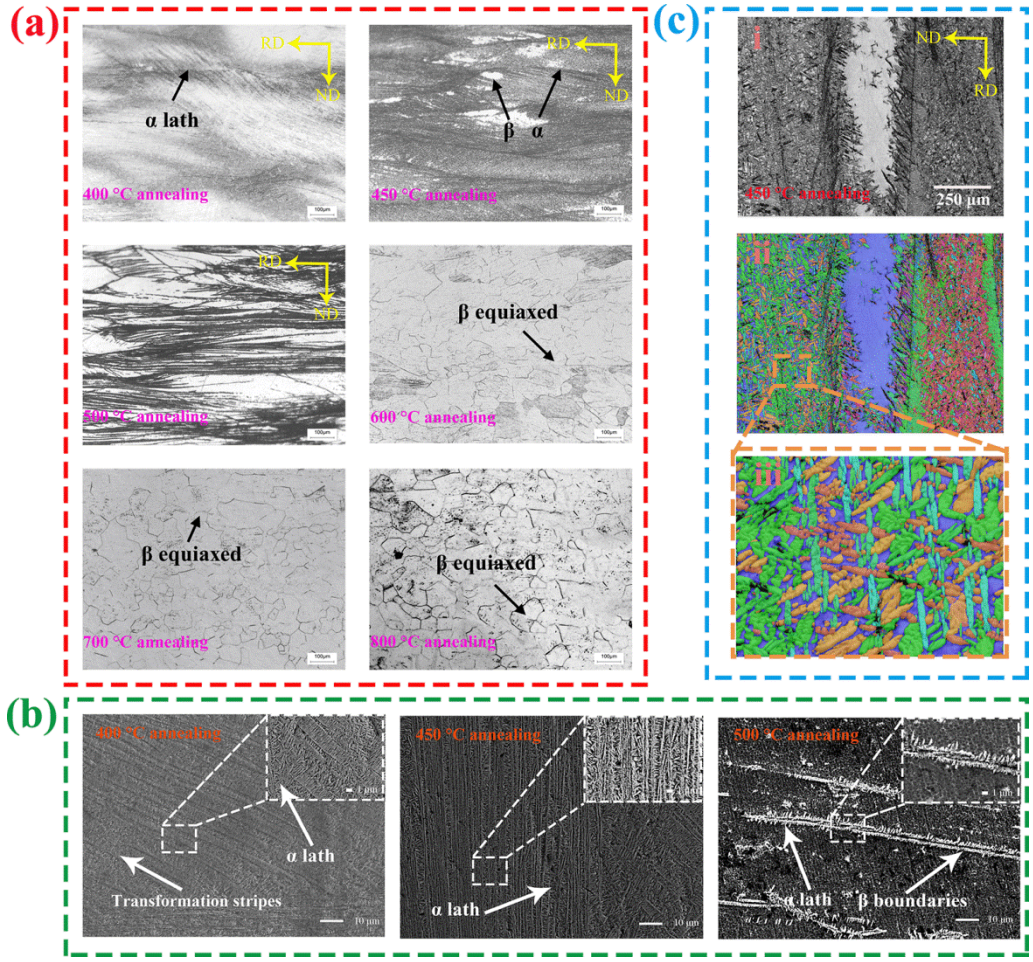

Figure 3. Microstructure of Zr–Ti–8V alloy in annealed condition: (**a**) OM, (**b**) SEM, (**c**) EBSD.

The annealed alloy was also tested by EPMA. Figure 4 shows the EPMA image of the annealed Zr–Ti–8V alloy by comparing the distribution of Zr, Ti, and V elements in the alloy matrix. The formation of evident V-rich regions in the matrix under 400 °C and 450 °C annealing conditions was found. Based on the metallographic analysis, the V-rich region appears to correspond to the unknown region in the metallographic diagram, while the V-rich region annealed at 400 °C is significantly larger than that at 450 °C. These outcomes are also consistent with the XRD test. Due to the application of a lower annealing temperature at 400 °C and a relatively short holding time, the atomic migration ability was reduced. Thus, the original β-phase in the alloy annealed at the temperature value of 400 °C could not be completely decomposed into the α-phase. A V-poor zone could be also found near the grain boundary at the annealing temperature of 500 °C, which was due to the preferential generation of the α phase near grain boundaries. We must emphasize that the α-phase belongs to the V-poor phase. By further increasing the annealing temperature in the range

of 600 °C to 800 °C, the elements were uniformly distributed, with no apparent elemental segregation taking place.

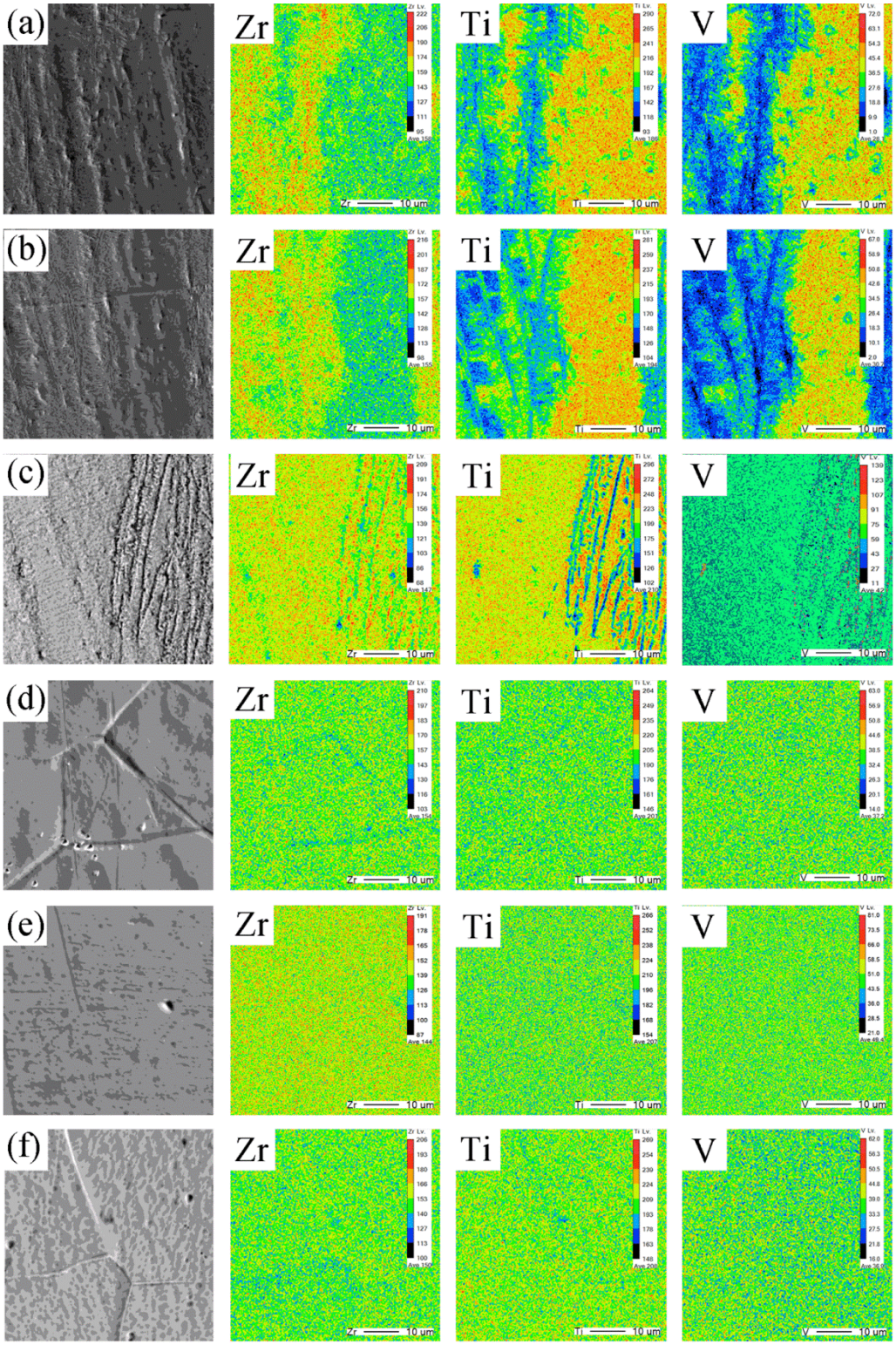

Figure 4. EPMA images of annealed Zr-Ti-8V alloys: (**a**) 400 °C; (**b**) 450 °C; (**c**) 500 °C; (**d**) 600 °C; (**e**) 700 °C; (**f**) 800 °C.

3.3. Mechanical Properties

3.3.1. Tensile Properties

The test results of the tensile mechanical properties of the Zr-Ti-8V alloy at different annealing temperatures are shown in Figure 5. As shown in Figure 5a, the elongation after fracture, yield strength, ultimate tensile strength, and modulus of elasticity of the alloy are significantly affected by the annealing temperature. Figure 6a–d shows the specific performance parameters. More specifically, the alloy annealed at the temperature value of 450 °C shows better mechanical properties, with an ultimate tensile strength of up to 1040 ± 12 MPa and elongation of up to 8.2 ± 0.3%. This is discussed in more detail below. Although the alloy annealed at 400 °C showed the highest ultimate compressive strength, poor elongation after the break was recorded. The compressive strength and elongation at break were 1417 ± 11 MPa, and 1.7 ± 0.2%, respectively. For the alloys annealed at 700 °C and 800 °C, a good elongation behavior after the break was observed, with elongation ranging from 11.4% to 11.5%. Compared with annealing at 450 °C, the ultimate tensile strength decreased significantly, which reflects the well-established mechanical rule that better elongation usually corresponds to a lower tensile strength. The alloy structures annealed at 500 °C and 600 °C exhibited poor ultimate tensile strength and poor post-extension, as shown in Table 1.

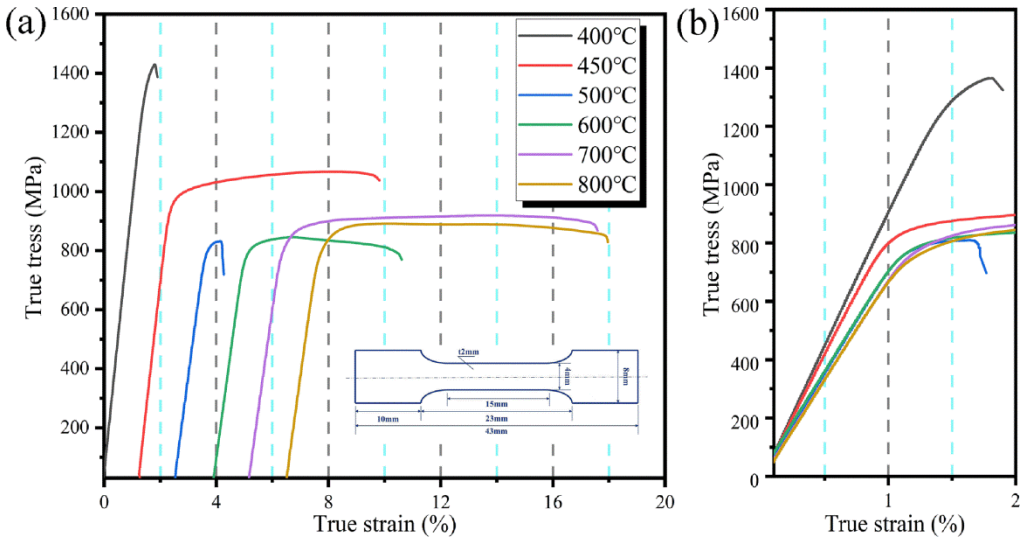

Figure 5. (**a**) True stress–strain curve and (**b**) elastic-deformation-stage true stress–strain curve of annealed Zr–Ti–8V alloys.

Table 1. Yield strength, compressive strength, elastic modulus, and elongation after fracture of the annealed Zr–Ti–8V alloys.

Alloys	400 °C	450 °C	500 °C	600 °C	700 °C	800 °C
Yield strength (MPa)	1408 ± (21)	966 ± (9)	810 ± (16)	809 ± (18)	868 ± (6)	839 ± (9)
Ultimate tensile strength (MPa)	1417 ± (11)	1040 ± (12)	846 ± (12)	856 ± (13)	915 ± (9)	893 ± (8)
Elastic modulus (GPa)	90 ± (1)	84 ± (2)	79 ± (6)	69 ± (2)	71 ± (1)	69 ± (3)
Elongation (%)	1.7 ± (0.2)	8.2 ± (0.3)	3.7 ± (1.7)	6.9 ± (0.3)	11.9 ± (0.5)	11.4 ± (0.8)

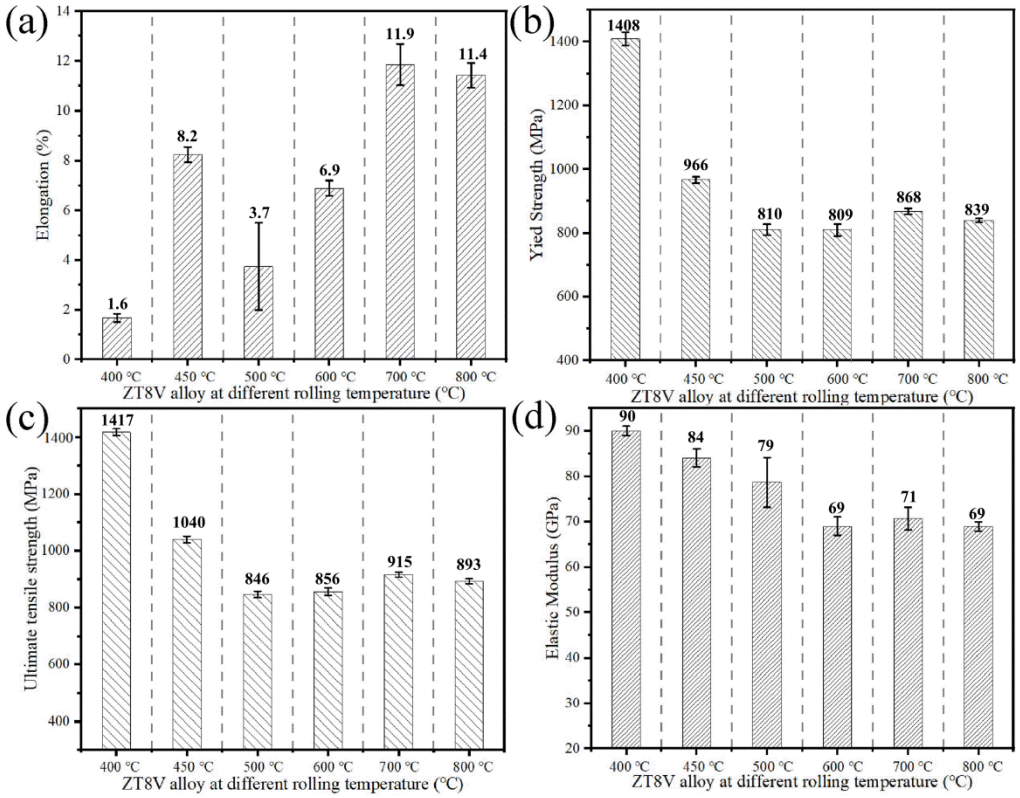

Figure 6. Elongation (**a**), yield strength (**b**), ultimate tensile (**c**) and modulus of elasticity (**d**) of annealed Zr–Ti–8V alloys.

Based on the trend curve of the elastic modulus with the applied annealing temperature in Figure 6d and analyzing the variation law of the elastic modulus of the alloy, when the annealing temperature is in the range of 400 °C to 600 °C, the elastic modulus of the alloy shows an opposite variation trend with the annealing temperature. On the other hand, when the annealing temperature is in the range of 600 °C to 800 °C, the modulus of elasticity of the alloy does not significantly change. By further observing the trend of the yield strength of the alloy as a function of the annealing temperature, a similar trend to that of the elastic modulus is found; the occurrence of such a change is related to the atomic bonding pattern.

Figure 7 shows the tensile fracture morphology of samples of the Zr–Ti–8V alloy with different annealing temperatures. Based on their sizes, the tough nests in the fractures of the alloys annealed at 450 °C, 700 °C, and 800 °C were large and deep, characteristic of ductile fracture. The fracture microscopic morphology shown in Figure 7c,d has a non-uniform size of tough nests and tiny cracks at the fractures can be observed, reflecting the low plasticity. Notably, the fracture microstructure of the alloy annealed at 400 °C exhibits very small toughness nests, which also indicates a poor plastic deformation capability in the alloy.

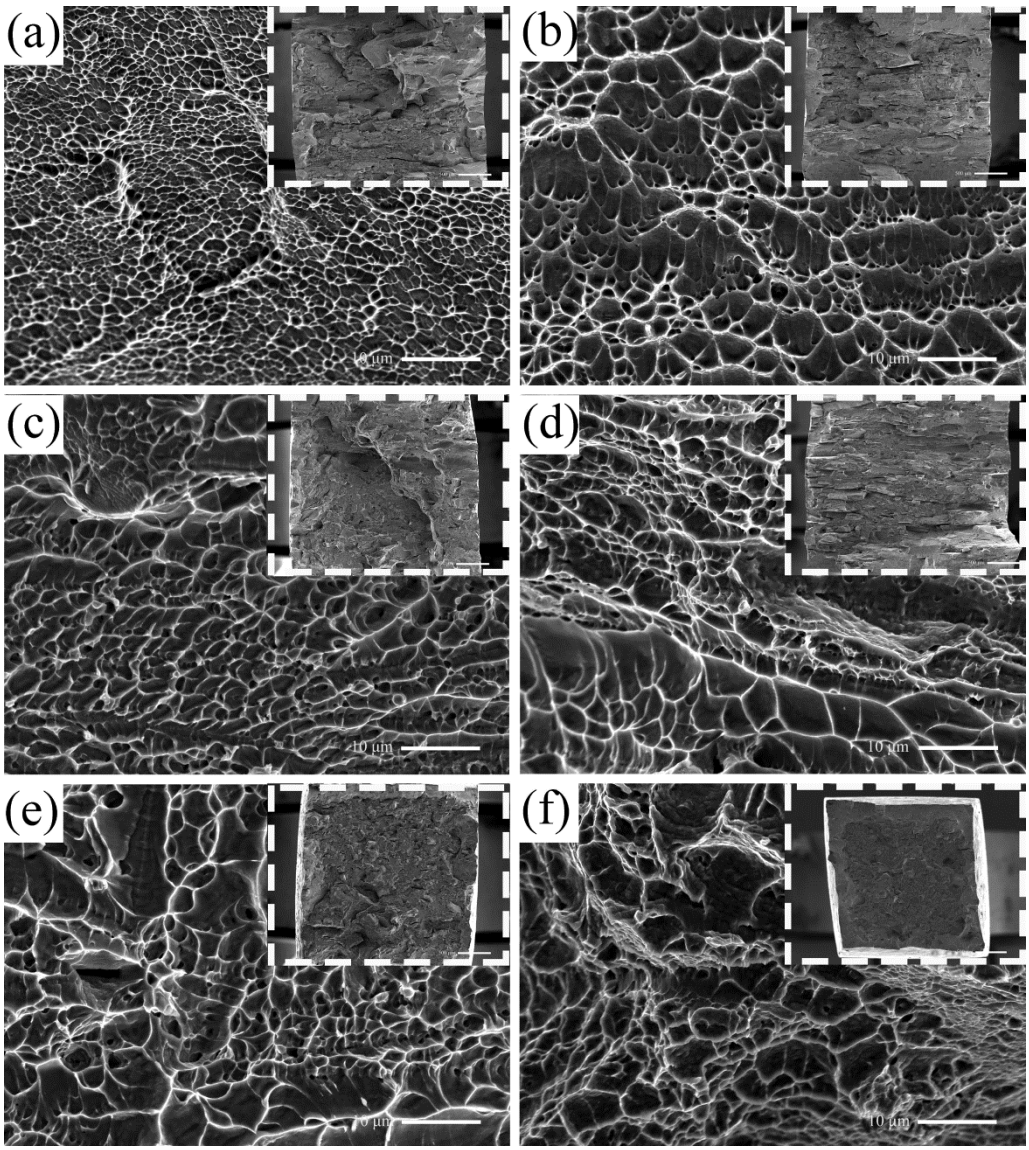

Figure 7. Fracture morphology of the annealed Zr–Ti–8V alloys: (**a**) 400 °C, (**b**) 450 °C, (**c**) 500 °C, (**d**) 600 °C, (**e**) 700 °C, (**f**) 800 °C; the inset picture shows the overall shape of the fracture.

3.3.2. Microhardness

In this work, the microhardness of the samples at different annealing temperatures was tested. Figure 8a shows the histogram of Vickers hardness test results of the Zr–Ti–8V alloy at different annealing temperatures. Interestingly, the alloy annealed at 400 °C showed the largest Vickers hardness (371 $HV_{1.96}$), and the temperature was further increased to 345 $HV_{1.96}$ at 450 °C, which was 26 $HV_{1.96}$ lower than that of the alloy annealed at 400 °C. In addition, the microhardness of the alloy annealed at the temperature range from 500 °C to 800 °C had a decreasing trend, but the decrease was not large. As a result, by considering the microhardness characteristics of the alloy in combination with the phase components, we concluded that the microhardness values of the α + β dual-phase alloy were higher than the β phase alloy.

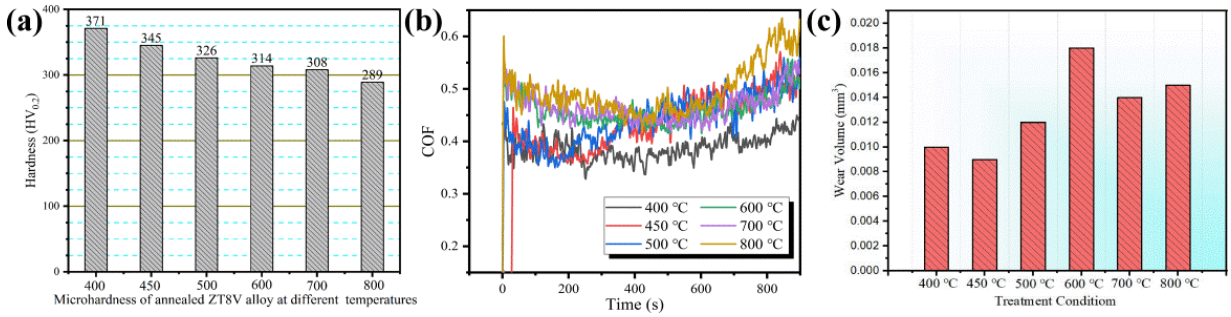

Figure 8. (**a**) Microhardness of the annealed Zr–Ti–8V alloys. (**b**) Frictional wear curves of samples at different annealing temperatures. (**c**) Wear volume of the annealed Zr–Ti–8V alloys.

3.3.3. Tribological Properties

The impact of the annealing temperature on the tribological properties of the Zr–Ti–8V alloy was further studied. To do so, frictional wear experiments were conducted on specimens with different annealing temperatures. The results of the friction coefficient curves are shown in Figure 8b, where the curves of the run and stage have been removed. Here, the friction coefficient of the alloy substrate that was annealed at 400 °C is relatively smooth from the beginning to the end, and they all remain around the value of 0.4. For the alloy substrates that were annealed at 450 °C and 500 °C, similar friction coefficients to annealing at 400 °C were recorded in the first 300 s, while the friction coefficients were around 0.4. After 300 s, the friction coefficients of both exhibited an increasing tendency with time, and by the end of the experiment, the same pattern was observed. The coefficient of friction of the alloy structures annealed within the range of 600–800 °C remained at a relatively high level (0.5) at the beginning of the experiment, and interestingly, a declining pattern in the 0–400 s time range emerged. After 400 s, the friction coefficient of the alloy increased with time. Comparison of the magnitude of the coefficients of friction at each stage of the alloys annealed at 600–800 °C revealed that the alloy annealed at 800 °C maintained a high coefficient of friction at all stages. Meanwhile, the alloys annealed at 600 °C and 700 °C possessed similar coefficient of friction curves.

The wear volume is regarded as a physical quantity indicator that can visually reflect the frictional wear performance; Figure 8c shows the wear volume of specimens annealed at different temperatures. The wear volume of the specimen annealed at 600 °C is the largest, namely 0.578 mm^3, which indicates that the wear resistance of the specimen annealed at 600 °C was poor and severe wear occurred during the frictional wear process. Consequently, the reduced volume left the substrate in the form of abrasive chips [29]. In striking contrast, the specimen annealed at 400 °C had the smallest wear volume, which was due to its higher hardness, denser film layer, and reduced number of defects, resulting in excellent wear resistance.

Since the friction process will inevitably induce the formation of many complex conditions such as the broken film of abrasive chips, damage to the grinding ball, etc., the impact of the friction coefficient on the results of friction wear is not clear. At this time, the two-dimensional and three-dimensional morphology of the abrasion marks can provide valuable evidence, as can be ascertained from Figure 9. The three-dimensional morphology of all the specimens shows a deep furrow-based shape along the direction of the ball movement, whereas many fine particles scattered near the furrow can be detected, which are typical of the abrasive wear morphology [30,31]. Grain wear also occurs when the micro-convex body between the two contacting surfaces is dislodged to form abrasive chips or when external hard particles are introduced, which can produce microscopic cuts on the surface and cause scratches. Thus, the abrasion marks could lead to the formation of a furrow-like shape. Comparing the two-dimensional images and cross-sectional curves depicted in Figure 9, the abrasion marks of the specimen annealed at 400 °C were narrower and shallower, and for the specimen annealed at 400–600 °C, they gradually became wider and deeper as

the annealing temperature was increased. Notably the wear marks were narrower and shallower within the range of 700–800 °C compared to the annealing temperature of 600 °C.

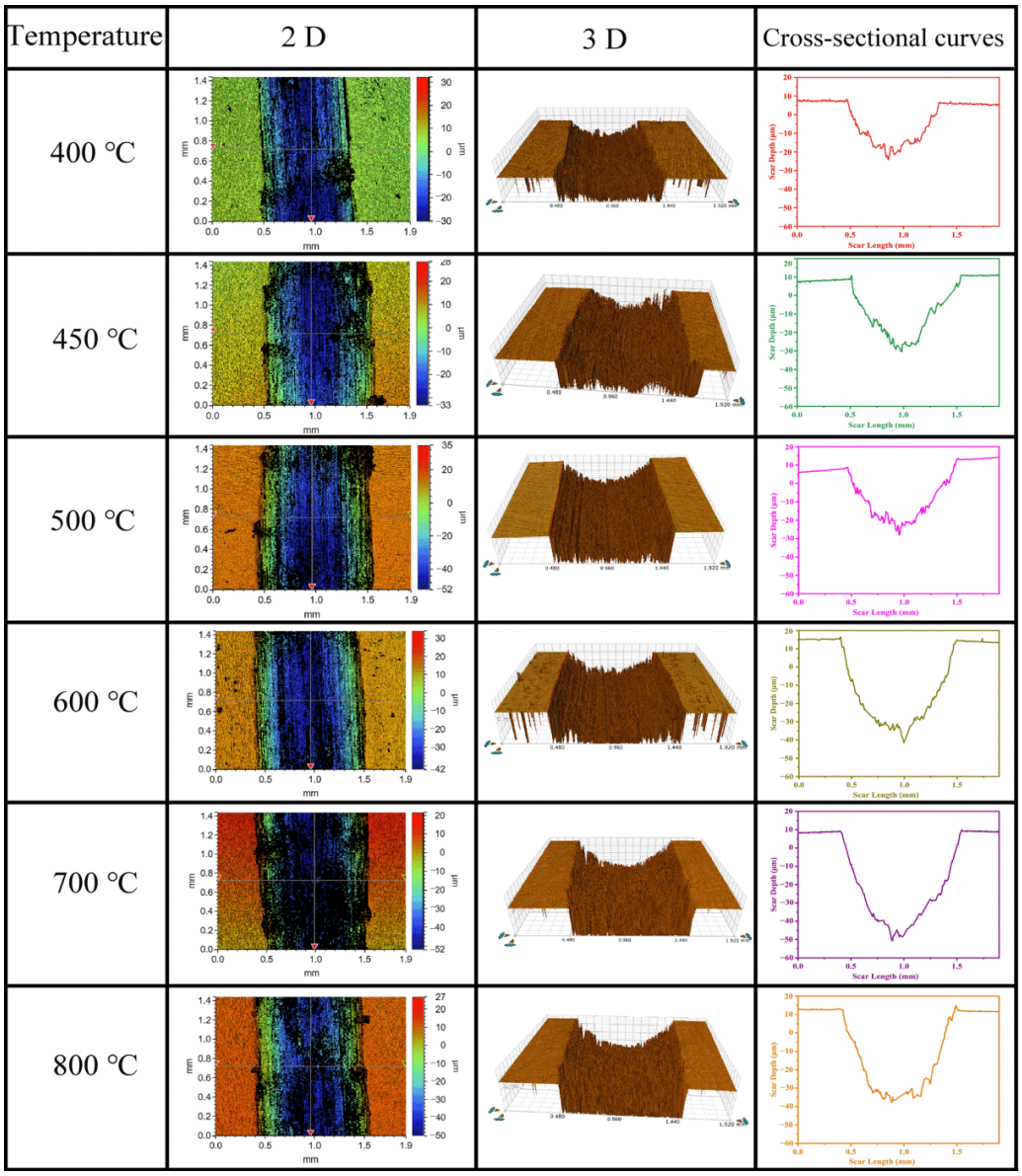

Figure 9. Two-dimensional and three-dimensional morphology of the annealed Zr–Ti–8V alloys.

4. Discussion

4.1. Tensile Performance Analysis

Figure 10 shows the strain-hardening rate versus the strain curve for the partially annealed Zr–Ti–8V alloy. The work-hardening rate reflects the real-time hardening rate during the deformation process of the material, and a higher value indicates the sensitivity of the material to work hardening. However, the work-hardening rate is also affected by external factors such as temperature and strain rate. Hence, it can only reflect the work-hardening ability of the material to a certain extent. Notably, the strain-hardening rate of all alloys decreased sharply in the first stage, which was mainly caused by the transition from the elastic to the plastic deformation mechanism of the alloy. During the second stage was the plastic deformation, where the strain-hardening rate of the alloy was affected by a variety of deformation mechanisms. As can be seen from the figure, the strain-hardening rate of the alloy in this stage remained unchanged, being parallel to the *x*-axis. The third stage could be assigned to the plastic deformation mechanism; the strain-hardening rate decreased slowly

in this stage. By comparing the magnitudes of the strain-hardening rate in the second phase, a higher value emerged for annealing at 450 °C than the other annealing temperatures. This effect clearly indicates that the alloy has a higher resistance to the plastic deformation mechanism when annealed at 450 °C. The dual-phase microstructure naturally induces additional strain-hardening compared to the individual constituent phases. During the deformation, the fine needle-like α-phase acted as a hard phase and impeded dislocation movement. The simultaneous enhancement of both strength and ductility caused by high strain-hardening has been also reported in several studies [32,33].

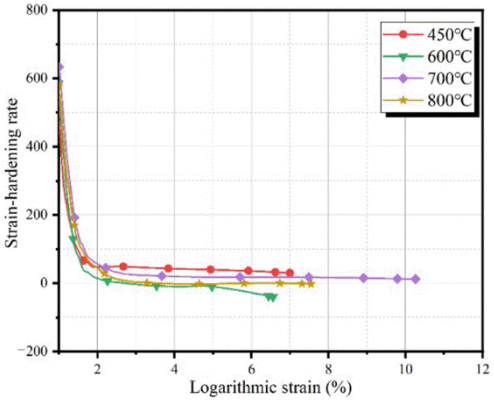

Figure 10. The compressive strain-hardening rate ($\Theta = d\sigma/d\varepsilon$) vs. the logarithmic strain of the studied alloys.

The phase composition and microstructure of the alloys were also characterized by significant changes in phase composition and microstructure by enforcing different annealing temperatures. The results of the tensile properties and hardness tests of the annealed Zr–Ti–8V alloy indicate that the mechanical properties of the proposed alloy configuration are sensitive to changes in the phase composition and microstructure. The fine-grain strengthening effect caused enhancement of the mechanical properties of the alloy by introducing a large number of grain boundary defects, which impeded the movement of dislocations. In addition, in contrast to the second-phase strengthening effect, fine-grain strengthening usually resulted in a better strength-to-plastic ratio [34]. During the tensile property tests, we also found that the α + β duplex alloys with less α-phase content usually exhibited poor mechanical properties. According to the literature, it has been demonstrated that duplex alloys usually exhibit excellent mechanical properties. By combining them with the microstructure of the alloy, the α-phase preferentially precipitates at grain boundaries. As a result, an unstable alloy structure is formed that is prone to stress concentration [35,36]. Cavity nucleation, growth, and agglomeration can also lead to crack formation, which then propagates along regions with high stress concentration or weak regions (grain boundaries, two-phase particles, shear zones), causing crack generation and subsequent rapid propagation that ultimately contribute to the poor plastic deformability of the alloy [32].

In the Zr–Ti–8V alloy annealed at 450 °C, the β-phase was decomposed into α-phase in large quantities at the annealing temperature, while the α-phase was uniformly distributed and dominated in the alloy matrix. The α-phase was composed of a dense hexagonal (HCP) structure with fewer slip surfaces in the crystal. Thus, the α-alloy usually exhibited high mechanical strength and high hardness, while the uniform distribution of the α-phase ensured the structural stability of the alloy, making it less prone to developing stress concentrations [37]. This microstructure also gave the alloy good plastic deformation ability. Under enforced high-temperature annealing conditions, the alloy matrix could be found in the single β-phase, and the crystal structure was body-centered cubic (BCC), which has more slip surfaces. Consequently, the β-phase alloy usually had better plastic deformation ability [38]. In general, the strength of the alloy increased as the grain size decreased. By comparing the grain size of isometric grains of the alloy annealed at a relatively high temperature range

(600–800 °C), we found that the difference in the grain size was not large. Hence, the difference in the ultimate tensile strength and Vickers hardness also was not large.

4.2. Tribological Properties Analysis

A large frictional heat during friction is generated by a given substrate at a large sliding speed, which will inevitably accelerate the reaction between the air and the substrate and lead to the formation of a thin oxide layer on the substrate surface. The generation and breakage of the oxide layer during the friction process is considered a dynamic process: (1) Under the influence of frictional heat, a thin oxide layer is rapidly generated on the surface of the substrate. The oxide layer is relatively hard and can play a certain protective role for the substrate. (2) Under the impact of load and constant sliding friction, the oxide film generated by the frictional heat is poorly bonded to the substrate and thus breaks down to form tiny fragments of oxide particles [38].

The discharge of generated oxide particles during the friction process is difficult to achieve relative to time, producing secondary damage to the surface and imposing serious abrasive wear phenomena. Similarly, the oxide particles can scratch the hard counterbalance ball and cause adhesion effects, further aggravating the wear. The friction curves and the morphology of the wear grooves indicate the simultaneous manifestation of multiple wear mechanisms in experimental alloys. As Zr- and Ti-based alloys are chemically active and ductile, their wear mechanisms can be divided into the formation of transfer layers, work hardening, and oxidation of the material surface, with abrasive wear occurring on all experimental alloys under the combined effect of multiple wear mechanisms [39–41]. The local hardness (H) is usually associated with the sliding wear behavior of a material, where the amount of material lost to abrasive wear is inversely proportional to the hardness of the material, according to the following equation [42]:

$$V = KLS/H \quad (1)$$

where V is the wear volume, K is the coefficient of friction, L stands for the normal load during the wear test, S represents the sliding distance, and H is the local hardness. It can be seen from Equation (1) that the surface hardness of a material is closely related to its wear resistance. The hardness tests showed that the Zr–Ti–8V alloy had a high surface hardness when annealed within the range of 400–500 °C and therefore reflected a low wear volume. At the range of 600–800 °C, the Zr–Ti–8V alloy had a lower surface hardness, and the full β alloy showed good ductility. As a result, severe adhesive wear occurred in the later part of the experiment, increasing the wear level, which was the underlying reason for the increase in the friction coefficient of the alloy (400–900 s). Interestingly, the alloy annealed at 600 °C has the highest wear volume loss of all the annealed alloys, but it was harder than the alloy annealed at 700–800 °C. This phenomenon can be attributed to the instability of the grain size. On the one hand, the large difference in the grain size, in terms of length, and the uneven distribution of grains within the matrix during annealing at 600 °C can lead to severe plastic deformation in the large grain region during frictional wear, which further aggravates adhesive wear. On the other hand, the work-hardening phenomenon was prominent under large plastic deformation conditions, resulting in a higher hardness in this region than in the fine-grained zone. The development of uneven forces can also lead to the formation of cracks within the alloy, prompting the dislodging of particles.

We must emphasize here that when the particles are dislodged during the wear process, they can produce abrasive wear. Figure 11 depicts more clearly the friction wear microstructure of the two different alloy configurations. The friction coefficient curves show a gradual decrease in the early stages of the experiment, mainly due to the generation of a large amount of heat on the surface under high-speed friction conditions, which could lead to the formation of a dense and hard oxide film on the surface. In the later stages of the experiment, the coefficient of friction of all alloys increased to varying degrees, mainly due to fatigue failure of the alloy surface under prolonged friction conditions, as the hard oxide film peeled off and the surface began to become rough. We regard the hardness of

the alloy as the main factor influencing the wear resistance of the alloy, followed by the microstructure of the alloy. In this study, the alloy phase composition and microstructure were regulated by applying different annealing temperatures to experimentally control the alloy's wear resistance.

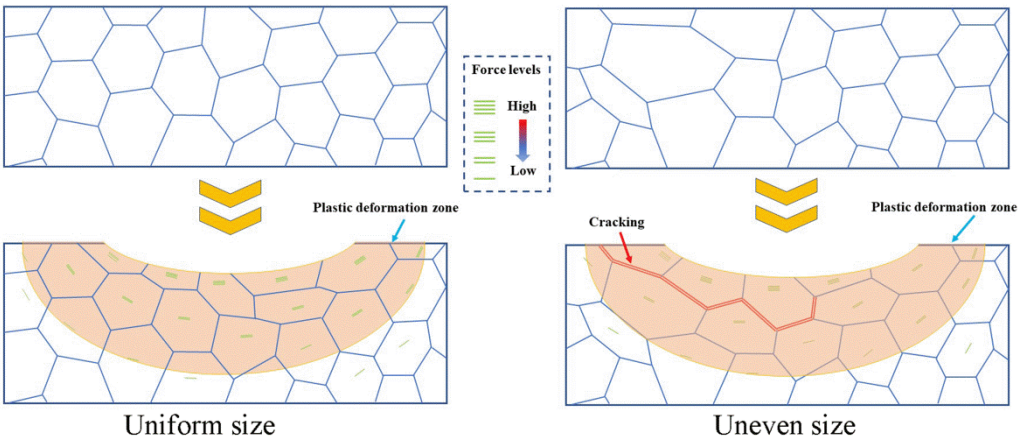

Figure 11. Two different microstructure wear models.

5. Conclusions

In this study, the impact of different annealing temperatures on the structure and mechanical properties of the Zr–Ti–8V alloy were thoroughly investigated with a variety of experimental methods to obtain the following conclusions:

1. The hot-rolled Zr–Ti–8V alloy was annealed at lower temperature values (400–500 °C), and the alloy consisted mainly of α + β phases. The needle-like alpha tissue was regularly distributed in the matrix with the deformed fibrous tissue. When annealed at 500 °C, a small amount of needle-like α phase precipitated on both sides of the grain boundary, resulting in an organization of coarse-grain boundaries. When the annealing temperature was increased above 600 °C, a large number of equiaxed β grains with uniform grain size and small dimensions appeared. The grain size of the alloy initially showed a decreasing trend and then increased as the annealing temperature increased.
2. The tensile properties of the alloy were significantly affected by the annealing temperature. More specifically, at 400 °C, the alloy had high tensile strength (1417 MPa), but its plasticity was poor at 1.7%, while at 450 °C, the alloy exhibited the best strength–plastic ratio (1039 MPa, 8.2%). The dual-phase microstructure naturally induced additional strain-hardening compared to the individual constituent phases. As the annealing temperature continued to increase, the alloy structure became a single β equiaxed crystal, the strength of the alloy decreased, and the plasticity was significantly enhanced.
3. Hardness and friction wear tests on alloys with different annealing temperatures revealed that the hardness and wear resistance of the alloys were sensitive to their phase composition. The alloys with a α + β dual-phase organization exhibited higher hardness and wear resistance. The highest hardness and best wear resistance were extracted for the alloy annealed at 400 °C. On the other hand, the single-β alloys had lower hardness and wear resistance, while for the single-β-phase alloys annealed at 700 °C, good wear resistance was recorded.

Author Contributions: Y.L., K.C., T.S.: Conceptualization, methodology, original draft writing. B.C.: Data curation, investigation. C.X. and Q.L.: Supervision, validation. All authors have read and agreed to the published version of the manuscript.

Funding: This work was supported by the National Natural Science Foundation of China (Grant No. 52071126, 52125405), the National Key R&D Program of China (Grant No. 2018YFA0703602),

the Central Guidance on Local Science and Technology Development Fund of Hebei Province (226Z1009G), and the Foundation Strengthening Program (No: 2019-JCJQ-00).

Data Availability Statement: The data used to support the findings of this study are included within the article.

Conflicts of Interest: The authors declare that they have no known competing financial interest or personal relationship that could have appeared to influence the work reported in this paper.

References

1. Zhou, W.H.; Duan, F.H.; Meng, Y.H.; Zheng, C.C.; Chen, H.M.; Huang, A.G.; Wang, Y.X.; Li, Y. Effect of alloying oxygen on the microstructure and mechanical properties of Zr-based bulk metallic glass. *Acta Mater.* **2021**, *220*, 117345. [CrossRef]
2. Baêta, D.A.; Costa, D.J.R.; Cardoso, F.G.; Medeiros, N. Evaluation of fretting wear occurrence on the surface of nuclear fuel rods of Zr–1Nb–1Sn-0.1Fe alloy: Effects of assembly misalignment and grid spring loading. *Wear* **2020**, *460–461*, 203422. [CrossRef]
3. Feng, Z.H.; Jiang, X.J.; Zhou, Y.K.; Xia, C.Q.; Liang, S.X.; Jing, R.; Zhang, X.Y.; Ma, M.Z.; Liu, R.P. Influence of beryllium addition on the microstructural evolution and mechanical properties of Zr alloys. *Mater. Des. (1980–2015)* **2015**, *65*, 890–895. [CrossRef]
4. Feng, Z.H.; Xia, C.Q.; Jiang, X.J.; Liu, S.G.; Zhang, X.; Zhang, X.Y.; Ma, M.Z.; Liu, R.P. Investigating the structure-property correlation of a novel Zirconium alloy by annealing treatment. *Mater. Sci. Eng. A* **2016**, *677*, 393–399. [CrossRef]
5. Liu, J.; Yu, H.; Karamched, P.; Hu, J.; He, G.; Goran, D.; Hughes, G.M.; Wilkinson, A.J.; Lozano-Perez, S.; Grovenor, C.R.M. Mechanism of the α-Zr to hexagonal-ZrO transformation and its impact on the corrosion performance of nuclear Zr alloys. *Acta Mater.* **2019**, *179*, 328–341. [CrossRef]
6. Huang, J.; Zou, S.; Xiao, W.; Yang, C.; Yu, H.; Zhang, L.; Zhang, K. Microstructural evolution of Cr-coated Zr-4 alloy prepared by multi-arc ion plating during high temperature oxidation. *J. Nucl. Mater.* **2022**, *562*, 153616. [CrossRef]
7. Zhang, X.; Chen, Y.; Hu, J. Recent advances in the development of aerospace materials. *Prog. Aerosp. Sci.* **2018**, *97*, 22–34. [CrossRef]
8. Adamson, R.B.; Coleman, C.E.; Griffiths, M. Irradiation creep and growth of zirconium alloys: A critical review. *J. Nucl. Mater.* **2019**, *521*, 167–244. [CrossRef]
9. Liu, S.G.; Ma, W.; Zhang, X.; Xia, C.Q.; Luo, H.L.; Zhang, X.Y.; Ma, M.Z.; Liu, R.P. Microstructure design and mechanical properties of annealed TiZrAlB alloys. *Mater. Lett.* **2020**, *260*, 126910. [CrossRef]
10. Tewari, R.; Srivastava, D.; Dey, G.K.; Chakravarty, J.K.; Banerjee, S. Microstructural evolution in zirconium based alloys. *J. Nucl. Mater.* **2008**, *383*, 153–171. [CrossRef]
11. Zhang, X.; Zhang, B.; Liu, S.G.; Zhang, X.Y.; Ma, M.Z.; Liu, R.P. Microstructure and mechanical properties of novel Zr–Al–V alloys processed by hot rolling. *Intermetallics* **2020**, *116*, 106639. [CrossRef]
12. Fan, Q.; Yuan, B.; Xie, M.; Shi, M.; Zhou, J.; Yang, Z.; Zhao, W. Effects of hot rolling temperature and aging on the second phase particles of Zr-Sn-Nb-Fe zirconium alloy. *Nucl. Mater. Energy* **2019**, *20*, 100700. [CrossRef]
13. Feng, Z.; Liu, Z.; Li, J.; Dong, H.; Zhong, H.; Lu, H.; Wang, J.; Zhang, X. Microstructure evolution behavior and mechanical mechanisms in a near α-Zr alloy by cold rolling. *J. Alloys Compd.* **2022**, *907*, 164425. [CrossRef]
14. Wei, T.; Dai, X.; Long, C.; Sun, C.; Long, S.; Zheng, J.; Wang, P.; Jia, Y.; Zhang, J. Comparison on the microstructure, aqueous corrosion behavior and hydrogen uptake of a new Zr-Sn-Nb alloy prepared by different hot rolling temperature. *Corros. Sci.* **2021**, *192*, 109808. [CrossRef]
15. Rogachev, S.O.; Sundeev, R.V.; Nikulin, S.A. Effect of severe plastic deformation by high-pressure torsion at different temperatures and subsequent annealing on structural and phase transformations in Zr-2.5% Nb alloy. *J. Alloys Compd.* **2021**, *865*, 158874. [CrossRef]
16. Chen, J.; Jiang, Y.; Liu, H.; Yi, D.; Zhang, R.; Dai, X.; Li, S.U. Texture evolution of cold-rolled Zr-1Sn-0.3Nb-0.3Fe-0.1Cr alloy during annealing. *J. Nucl. Mater.* **2019**, *524*, 226–238. [CrossRef]
17. Li, S.; Luan, B.; Liao, Z.; Liu, Z.; Chu, L.; Wen, S.; Murty, K.L.; Liu, Q. Effect of friction stir processing and subsequent annealing on microstructure and mechanical properties of a metastable β-Zr alloy. *Mater. Sci. Eng. A* **2021**, *822*, 141660. [CrossRef]
18. Yang, Z.N.; Wang, X.B.; Liu, F.; Zhang, F.C.; Chai, L.J.; Qiu, R.S.; Chen, L.Y. Effect of intercritical annealing temperature on microstructure and mechanical properties of duplex Zr-2. *5Nb alloy. J. Alloys Compd.* **2019**, *776*, 242–249. [CrossRef]
19. Yang, Z.; Liu, F.; Yan, Z.; Zhang, F. Effect of Annealing on Microstructure and Hardness of Hot and Cold Rolled Zr705. *Rare Met. Mater. Eng.* **2013**, *42*, 254–258. [CrossRef]
20. Fomin, A. Functionally graded zirconium oxide coatings produced on zirconium using induction heat treatment. *Compos. Struct.* **2019**, *220*, 318–323. [CrossRef]
21. Wang, Z.; Zhou, Y.; Wang, H.; Li, Y.; Huang, W. Tribocorrosion behavior of Ti-30Zr alloy for dental implants. *Mater. Lett.* **2018**, *218*, 190–192. [CrossRef]
22. Ding, Y.; Liu, S.; Xia, C.; Zou, X.; Liu, D.; Wang, Y.; Yang, T.; Li, Q. Thermal oxidation of novel Zr–Ti–Al–V alloy with high strength and toughness and its influence on the corrosion behavior. *Surf. Coat. Technol.* **2021**, *423*, 127576. [CrossRef]
23. Wang, B.L.; Li, L.; Zheng, Y.F. In vitro cytotoxicity and hemocompatibility studies of Ti-Nb, Ti-Nb-Zr and Ti-Nb-Hf biomedical shape memory alloys. *Biomed. Mater.* **2010**, *5*, 044102. [CrossRef]

24. Aldeen, A.W.; Chen, Z.W.; Disher, I.A.; Zhu, Y.; Yan, K. Growth kinetics of second phase particles in N36 zirconium alloy: Zr–Sn–Nb–Fe. *J. Mater. Res. Technol.* **2022**, *17*, 2038–2046. [CrossRef]
25. Wang, H.-Y.; Lu, S.-S. Study on thermal properties of phase change material by an optical DSC system. *Appl. Therm. Eng.* **2013**, *60*, 132–136. [CrossRef]
26. Marchetti, M.; Fois, M.; Ibos, L.; Dumoulin, J.; Bourson, P.; Piau, J.M. Comparative study in the identification of liquid to solid transition phase with DSC, Raman spectra analysis and chemiometrics methods applied to phase change materials used for icing-delay in civil engineering infrastructures. *Appl. Therm. Eng.* **2018**, *130*, 49–61. [CrossRef]
27. Fomin, A.; Voyko, A.; Fomina, M.; Mokrousov, S.; Koshuro, V. Functionally graded Ti(C,N) coatings and their production on titanium using solid-state carburization associated with induction heat treatment. *Compos. Struct.* **2020**, *245*, 112393. [CrossRef]
28. Koshuro, V.; Fomina, M.; Voyko, A.; Rodionov, I.; Zakharevich, A.; Skaptsov, A.; Fomin, A. Surface morphology of zirconium after treatment with high-frequency currents. *Compos. Struct.* **2018**, *202*, 210–215. [CrossRef]
29. Chirico, C.; Romero, A.V.; Gordo, E.; Tsipas, S.A. Improvement of wear resistance of low-cost powder metallurgy β-titanium alloys for biomedical applications. *Surf. Coat. Technol.* **2022**, *434*, 128207. [CrossRef]
30. Cui, W.F.; Shao, C.J. The improved corrosion resistance and anti-wear performance of Zr–xTi alloys by thermal oxidation treatment. *Surf. Coat. Technol.* **2015**, *283*, 101–107. [CrossRef]
31. Samuel, S.; Nag, S.; Scharf, T.W.; Banerjee, R. Wear resistance of laser-deposited boride reinforced Ti-Nb–Zr–Ta alloy composites for orthopedic implants. *Mater. Sci. Eng. C* **2008**, *28*, 414–420. [CrossRef]
32. Shokrani, A.; Al-Samarrai, I.; Newman, S.T. Hybrid cryogenic MQL for improving tool life in machining of Ti-6Al-4V titanium alloy. *J. Manuf. Process.* **2019**, *43*, 229–243. [CrossRef]
33. De Formanoir, C.; Martin, G.; Prima, F.; Allain, S.Y.P.; Dessolier, T.; Sun, F.; Vivès, S.; Hary, B.; Bréchet, Y.; Godet, S. Micromechanical behavior and thermal stability of a dual-phase α+α′ titanium alloy produced by additive manufacturing. *Acta Mater.* **2019**, *162*, 149–162. [CrossRef]
34. Feng, Z.H.; Li, D.; Dong, H.C.; Li, J.H.; Su, R.; Wu, D.Y.; Chen, Y.Q.; Zhang, X.Y.; Liu, R.P. Evolution of β phase and mechanical mechanisms in an α-type Zr alloy processed by rolling at different temperatures. *Mater. Charact.* **2021**, *172*, 110873. [CrossRef]
35. Wang, Y.; Chai, L.; Zhang, F.; Chen, K.; Guan, H.; Luo, J.; Li, Y. Effects of β-cooling rates on microstructural characteristics and hardness variation of a dual-phase Zr alloy. *Int. J. Refract. Met. Hard Mater.* **2021**, *100*, 105619. [CrossRef]
36. Kang, L.; Yang, C. A Review on High-Strength Titanium Alloys: Microstructure, Strengthening, and Properties. *Adv. Eng. Mater.* **2019**, *21*, 1801359. [CrossRef]
37. Li, Q.; Chen, K.; Xia, C.; Chen, B.; Liu, S.; Yang, T.; Liu, D.; Wang, Y.; Zhang, X. Microstructure evolution, mechanical properties, and corrosion behavior of novel Zr–Ti–V alloys. *Mater. Sci. Eng. A* **2021**, *817*, 141358. [CrossRef]
38. Kheradmandfard, M.; Kashani-Bozorg, S.F.; Kang, K.-H.; Penkov, O.V.; Hanzaki, A.Z.; Pyoun, Y.-S.; Amanov, A.; Kim, D.-E. Simultaneous grain refinement and nanoscale spinodal decomposition of β phase in Ti-Nb-Ta-Zr alloy induced by ultrasonic mechanical impacts. *J. Alloy. Compd.* **2018**, *738*, 540–549. [CrossRef]
39. Hua, K.; Wan, Q.; Zhou, Z.; Zhou, Q.; Li, X.; Wu, H.; Wang, H. Enhanced wear-resistance of TiZrHfNb refractory high entropy alloys meditated by subsurface instabilities. *Mater. Lett.* **2022**, *311*, 131612. [CrossRef]
40. Luo, J.; Sun, W.; Duan, R.; Yang, W.; Chan, K.C.; Ren, F.; Yang, X.-S. Laser surface treatment-introduced gradient nanostructured TiZrHfTaNb refractory high-entropy alloy with significantly enhanced wear resistance. *J. Mater. Sci. Technol.* **2022**, *110*, 43–56. [CrossRef]
41. Grigoriev, S.; Vereschaka, A.; Milovich, F.; Migranov, M.; Andreev, N.; Bublikov, J.; Sitnikov, N.; Oganyan, G. Investigation of the tribological properties of Ti-TiN-(Ti,Al,Nb,Zr)N composite coating and its efficiency in increasing wear resistance of metal cutting tools. *Tribol. Int.* **2021**, *164*, 107236. [CrossRef]
42. Shen, Z.; Lin, Z.; Shi, P.; Zhu, J.; Zheng, T.; Ding, B.; Guo, Y.; Zhong, Y. Enhanced electrical, mechanical and tribological properties of Cu-Cr-Zr alloys by continuous extrusion forming and subsequent aging treatment. *J. Mater. Sci. Technol.* **2022**, *110*, 187–197. [CrossRef]